

Autonomy Testbed Development for Satellite Debris Avoidance

E. Gregson, M. Seto

*Dalhousie University
Faculty of Engineering
Halifax, Nova Scotia, CANADA*

B. Kim

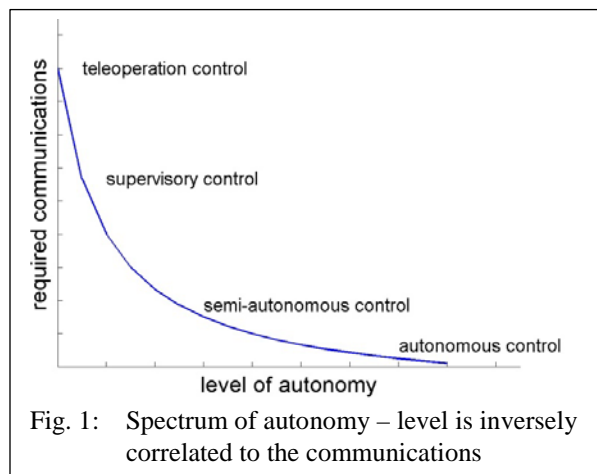
*Defence R&D Canada
Ottawa, Ontario, CANADA*

ABSTRACT

To assess the value of autonomy for spacecraft collision avoidance, a testbed was developed to model a typical low earth orbit satellite, the Canadian Earth-observation satellite RADARSAT-2. The testbed captures orbital and attitude dynamics, including J_2 gravitational, drag and solar radiation pressure perturbation forces and gravity gradient, drag, solar radiation pressure and magnetic torques. The modelled satellite has a GPS for position sensing and a gyro, magnetometer, two Sun sensors and two star trackers for attitude sensing. Its attitude actuators are reaction wheels and magnetorquers. A thruster model has been integrated. The testbed satellite uses Extended Kalman Filters for position and attitude state estimation. A nonlinear proportional-derivative controller is used to control the reaction wheels. The magnetorquers are controlled by the B-dot algorithm for de-tumbling. Tests performed with the testbed showed that it achieved comparable position and attitude determination accuracy to RADARSAT-2. Attitude control accuracy was not equal to RADARSAT-2 but was close enough to suggest a comparable accuracy could be attained with more tuning or the addition of an integral term. Magnetorquer detumbling appears to work. An orbital maneuver planner was implemented with a linear programming formulation. The testbed was applied to some preliminary autonomous collision avoidance problems to determine fuel consumption as a function of warning times prior to a collision. An algorithm was also presented based on in-situ detection of very small debris that future work will be based on.

1. INTRODUCTION

Spacecraft operate in the dynamic and harsh space environment where they are exposed to extreme temperatures, radiation and the potential for collision with space debris. Their ground control station (GCS) communications is limited to a few locations on Earth and they are to carry out their mission with limited GCS contact. This is the issue of communications latency. Thus, it is not always possible for the spacecraft to communicate, in a timely manner, with its GCS for an operator-driven response to an anomalous (unanticipated) event. Anomalous events can impact the mission in a permanent or transient manner. Increasing the spacecraft's on-board autonomy is one solution. The levels of autonomy are presented next to provide context on what 'autonomy' or autonomous control means here.



With a remote or teleoperated system the operator always controls it. With supervisory control, the operator has overall control but can transfer limited control over a specific function (e.g. change attitude). With semi-autonomous control, the system can accomplish a subset of its defined tasks without operator interaction and the operator completes the rest (e.g. orbital maneuver). In autonomous control the system accomplishes all its defined tasks without operator interaction. Automatic control, which is a scripted response, can be elements of supervisory or semi-autonomous control. Most satellites have this. Every satellite possesses some degree of autonomy to deal with periods when it is not in contact with its GCS like during detumbling or after serious

failures or faults. Satellites possess modes of operation which they autonomously switch between depending on circumstances. Satellites like RADARSAT-2 [1] and Sentinel-1 [2] have a *detumbling* mode, where the satellite runs its detumbling controller, *sun acquisition* mode for when the satellite has completed detumbling and needs to acquire an initial attitude, *nominal* mode when the satellite is operating normally and needs to track its nominal desired attitude, *safe hold* mode for when something has gone wrong and the satellite acquires the Sun, suspends its activities and communicates the problem to its GCS and awaits instructions and other modes related to *slows* and *attitude maneuvers*. The required communication frequency and bandwidth with the operator decreases with increase autonomy (Fig. 1). With the case of autonomous control, which is of interest here, the GCS would not interact with the satellite. The value of autonomous control is clear when the satellite has poor or intermittent communications with its GCS. From this point on, 'autonomy' refers to autonomous control.

With insight into the spacecraft's capabilities, configurations, environment, spacecraft-environment interactions and mission, the autonomy can reason about the anomalous event even if it was dynamic, has only partially observable spacecraft and environmental variables, and uncertainty in its sensor observations or adequacy of the observations. Towards this, the autonomy can process on-board sensor (or other) data into information and to use this newly generated in situ information to better achieve the system's mission goals. The information is used to make decisions to: alter or re-plan a mission; employ a different payload sensor; turn on/off non-critical systems; communicate with reduced bandwidth; collaborate with other systems (like the GCS) or implement remedies for on-board faults. For e.g., failure of a reaction wheel could be mitigated by switching to the spare reaction wheel (complete recovery) or re-tasking the control authority on the remaining reaction wheels (degraded recovery). Autonomy provides a reasoned response to an anomalous event with the intent to recover from the anomaly. The reasoning can also yield a longer-term prognosis that is considered in the autonomous recovery selected. The recovery action could be reactive (e.g. obstacle avoidance) or preventive (e.g. power redistribution due to a failed solar panel) [3]. Preventive recovery [4] requires autonomy. In all cases, a tool is needed to investigate the value of on-board autonomy for satellites.

The Dalhousie University and Defence R&D Canada, Ottawa Research Centre put joint effort to establish autonomous spacecraft operation research as part of the effort for Space Mission Assurance. The contribution of this paper is a very flexible testbed developed to model of a low earth orbit (LEO) satellite with RADARSAT-2 attributes and responses.

1.1 Autonomy on LEO Satellites

The value of the autonomy is its ability to address anomalous events where: (1) local space situational awareness is required (e.g. debris that cannot be detected with ground-based methods); (2) space weather makes GCS communications with the satellite difficult and (3) the anomalous event evolves too rapidly for a timely GCS analysis and response (e.g. late collision warning). For satellite debris avoidance, this could be a LEO low speed collision with debris that is less than 5-10 cm in size and in poor communications conditions due to space weather. In that event, the satellite would rely entirely on its on-board sensing and autonomy with little timely support from the GCS.

If the autonomy can respond to smaller scale debris, then this capability would complement ground-based methods. To achieve this, the satellite must locally detect smaller debris and respond to it. The detection may be possible with the on-board star tracker cameras, on-board sensors that are not widely implemented (e.g. space-based radar [5] or LIDAR), or other satellites. The autonomy could process the in-situ collected radar data into information; perform further calculations, optimizations and analysis with the information to yield a probability of collision; decide based on the probability of collision, re-plan the mission (orbital maneuver) then finally, actuate the new mission.

In LEO, ground-based radar and optical methods can detect in-orbit debris that is 5-10 cm or larger. Collision with debris this size can be catastrophic. At orbital speeds of 10 km / second, even smaller debris carry enough energy to damage or disable a satellite subsystem. In LEO, fly-bys with low relative velocities can be frequent due to the increased population of debris in Sun-synchronous orbits like with of RADARSAT-2. The time scales of these close-proximity motion are much longer – on the order of hours or days. Therefore, it is possible for the satellite to

detect neighboring objects and to plan and actuate an avoidance maneuver to maintain safe separation distances. At the latest, it is assumed that a satellite orbital adjustment for debris avoidance must be implemented 4 hours [6] prior to the time of closest approach (TCA) between satellite and debris. The actual maneuver change is in the form of an along-track firing of thrusters for a short time. This does not take long to actuate and reach steady state. An earlier orbital adjustment means a smaller applied Δv and hence less fuel is used. But, with an earlier adjustment the covariance (uncertainty) for the relative satellite-debris positions can change by the time of closest approach. However, when in situ detection is performed this bounds the uncertainty growth.

The autonomy could be implemented as follows: 1. resides completely on-board the satellite; 2. tools that GCS engineers can apply or, 3. as a hybrid of the two, i.e. distributed, to inform GCS decision-making and the subsequent actions to avoid a collision.

1.3 Testbed for Autonomy Assessment

A flexible testbed was required to study the value of the autonomy. The testbed would have to: model the physical satellite, its sensors and actuators; estimate the satellite and debris state (positions); implement satellite navigation and control and model the environment the satellite is in and the interaction of the satellite with its environment. Additionally, the testbed must accommodate the deliberation to run autonomous missions. The autonomy is a payload capability and if implemented, would reside on an additional processor(s) on the satellite, GCS or both. This distributed control is used by autonomous robots. The autonomy can be intricately and closely linked with all elements captured in the testbed. There are existing testbeds like STK SOLIS spacecraft simulator [7]. The spacecraft sensors, hardware and control loops, propulsion, communications and power can be modelled. However, the selection of hardware models and controllers are limited and cannot be customized. The '42' free software tools from NASA look promising as it allows a little more customization [8]. However, the structure to integrate a distributed payload autonomy capability was not as natural. The decision was made to create a new testbed that could accommodate the autonomy requirements. The testbed satellite motions are described by ordinary differential equations, so time histories are produced. The fusion between the prior, sensors, actuation, environment, etc. were achieved with Extended Kalman Filters (EKF).

The rest of this paper is structured as follows. The following sections describes the modelled satellite, its sensors and its actuators. Then, the satellite environment models are detailed. The satellite-environment interactions follow with sections on state estimation, navigation and control. Then illustrative examples from the testbed validation are presented. Finally, the benefit of on-board autonomy is briefly examined.

2. SATELLITE MODEL

As a satellite in a high-risk orbit for debris collision and the means to perform orbital maneuvers, RADARSAT-2 (Fig. 1) is an autonomous platform where autonomy might be applicable to low-speed collision avoidance. Information on RADARSAT-2 is available from [1], [6] and [9] (Table 1), however these sources do not have the detail for a dynamic RADARSAT-2 simulator. Information like the exact physical layout of the satellite's sensors and actuators, the guidance and control algorithms and hardware details were unavailable. As needed, educated guesses were made based on the satellite design requirements and similar satellites [2]. More detailed information was available for a European Space Agency (ESA) Earth observation satellite, Sentinel-2. [2] describes its attitude determination and control system and included the control algorithm, the modes that the satellite switches through and the hardware used. Sentinel-2 is a high pointing accuracy satellite similar in many ways to RADARSAT-2, so where there were uncertainties about RADARSAT-2's hardware or characteristics, information from Sentinel-2 was used.

When RADARSAT-2 was launched in 2007 with no collision avoidance strategy, it became clear that one was required. The GCS monitors the Space Track website with multiple tools to screen for future collisions and receives conjunction messages from the Joint Space Operations Center. The decision on whether to perform a maneuver depends on the assessed probability of collision. RADARSAT-2 has performed 11 collision avoidance maneuvers from 2010 – 2016 [6]. There is motivation to consider autonomous collision avoidance.

The testbed uses a 4th order Runge-Kutta method to integrate the orbital and attitude equations of motion. Attitude integration uses the same time step as orbit integration; in each cycle, both disturbance forces and torques are calculated, and the orbital state vector, $[\mathbf{r} \ \mathbf{v}]^T$, and attitude state vector, $[\boldsymbol{\omega}_{BG} \ \mathbf{q}]^T$, for the next cycle are determined. The models used for the satellite's components will be presented next. Table 2 is a summary of this.

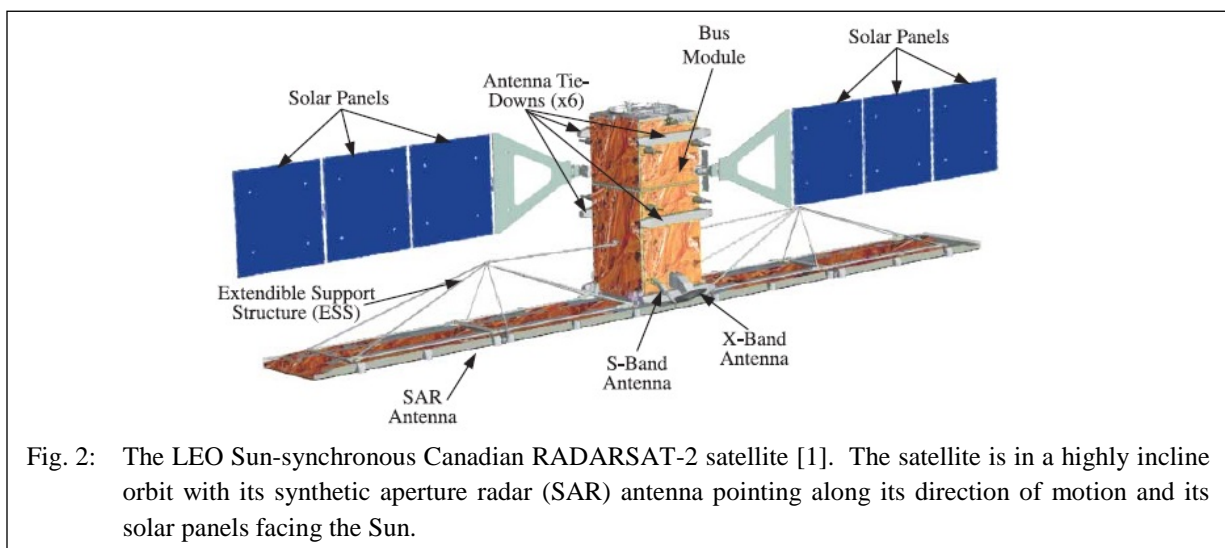
3. SATELLITE SENSOR MODELS

3.1 Gyroscope

The gyroscope model is Eq. (3.1). It is commonly used for simulating spacecraft attitude control hardware [10] [11]. The actual gyroscope used on RADARSAT-2 was unknown. Therefore, the model gyroscope was assumed to be the less precise of the two inertial measurement units on-board Sentinel-2 [2]. This sensor has been used on numerous space missions and is likely like the one used on RADARSAT-2 [12]. The gyroscope is assumed to always provide a measurement (unlike other sensors), up to frequencies well above those used for the measurements in the testbed

Table 1: Summary of physical RADARSAT 2 quantities modelled in the testbed

physical characteristics	mass	2300 kg
	spacecraft bus	1.34 m × 1.34 m × 3.2 m
	SAR antenna	15 m × 1.5 m
	SAR antenna mass	700 kg
	solar panel array	3.73 × 1.8 m
position control	6× thrusters	1 N (f) each
position determination	GPS	3σ accuracy of ± 60 m
	post-processed accuracy	3σ accuracy of ± 15 m
attitude determination	fusion of: 4-axis gyro, 3-axis magnetometer, 2× sun sensors, 2× star trackers	3σ accuracy of ± 0.02° for each axis
attitude control	4× reaction wheels (1 extra), 3× magnetorquers	3σ accuracy of ± 0.05°



3.2 Magnetometer

The three-axis magnetometer model in Eq. (3.2) does not return a reading if the magnetic moment of any of the magnetorquers is larger in magnitude than their residual moment value, because it is assumed the torquer field will corrupt the measurement. Without knowing the specific magnetometer used on RADARSAT-2, the specifications of the magnetometer from Sentinel-2 were used instead. The magnetometer on Sentinel-1 was a ZARM Technik FGM-A-75 [2]. It has a range of $\pm 75 \mu\text{T}$, and an accuracy of 0.5% [13]. Based on this the value of σ_b was set to $0.375 \mu\text{T}$.

3.3 Sun Sensors

RADARSAT-2 has two Sun sensors. The locations of RADARSAT-2's Sun sensors was unknown, so it was assumed one sensor was located on the $+Y$ face of the spacecraft central bus, and one on the $-Y$ face. This assumption means that one Sun sensor would be illuminated during nominal operation, and the two sensors together would cover essentially the entire celestial sphere. Since the Sun sensors are primarily used for Sun acquisition when the attitude is unknown (e.g. after detumbling), this seemed reasonable.

3.4 Star Trackers

Based on [6] and [14], the two star trackers used on RADARSAT-2 are likely the Leonardo A-STR autonomous star tracker. Their locations on the spacecraft were unknown. Each star tracker returns a quaternion representing its orientation, q_{SCIST} , and a 3×3 covariance matrix, R_{ST} for the Euler error angles [10]. The star tracker in the testbed was modeled to return the quaternion for the rotation from the satellite centered inertial (SCI) frame to the body frame.

The standard deviations of the error angles for the A-STR depend on the angular rate of the spacecraft. At higher rates, they are less accurate, and above a certain rate, they do not return a value because they cannot match an image. [15] lists the 3σ error angles for the A-STR given the angular rate. Above $2^\circ/\text{s}$, the star tracker does not return a value. The true angular velocity is supplied to the star tracker model to check this condition. The A-STR has a FOV of 16.4° [15]. If the Sun or the Earth are within the star tracker's FOV, it will not return a measurement. The two star trackers are assumed to be on the $+x$ and $+z$ faces of the central bus. These locations image the stars without the Earth or Sun in their FOV during RADARSAT-2 operation, including the 29.8° rolls to image on both sides of the ground track.

3.5 Global Positioning System

The position accuracy of RADARSAT-2 using the GPS measurements before processing was $\pm 60 \text{ m}$ (3σ). To simulate the GPS, a vector of Gaussian noise with a standard deviation of 20 m was added to the true position. The testbed GPS always provides a measurement, which is likely unrealistic. In the future, the model will be adjusted so that the GPS does not return measurements under certain conditions (e.g. incorrect satellite attitude or angular velocity too high). Further research will have to be done to determine what those conditions are.

4. SATELLITE ACTUATOR MODELS

4.1 Reaction Wheels

[16] approximately models the dynamics of a reaction wheel. A feature of this model was that as the wheel approaches its maximum speed, the torque available from the wheel approaches zero. It also models the relationship between the duty cycle of the control pulses applied to the wheel and the electromotive force on the wheel. The model assumed an AC two-phase induction motor driven by square pulses from the wheel's electronics based on an input voltage, V . It included the effects of friction in the wheel, a dead band in the input voltage and if the voltage's absolute value falls below a threshold, no pulses are generated. The net torque on the wheel is given by Eq. (4.1).

For each wheel at each simulation time step, the speed of the wheel and its moment of inertia J_w were used to calculate the wheel's angular momentum for the attitude dynamics equations. The torque requested by the control system was used as the actual wheel torque (assuming the wheel is capable given friction and nonlinearities) calculated from the wheel speed. The actual wheel torque was divided by the wheel moment of inertia to give the change in its speed.

4.2 Magnetorquers

For the testbed, it was assumed that the magnetic moment requested by the control system could be provided by the magnetorquers, up to their maximum magnetic moment. Based on the Sentinel-2 satellite's magnetorquers [13], this was 150 Am^2 [2]. It was also assumed the requested magnetic moment could be achieved instantly, but that it takes a finite time to fall to its residual level. Without knowing the magnetorquer's specific residual moment on RADARSAT-2 or Sentinel-2, the NewSpace System's magnetorquer were used [17]. This was a maximum moment of 100 Am^2 and a residual moment of 0.1 Am^2 . 0.1 Am^2 was the magnetorquer's residual moment in the testbed. Once the current to the magnetorquer was zero, the magnetic moment linearly decay to its residual value. The testbed magnetorquers take 0.1 seconds for the moment to decay from its maximum 150 Am^2 to 0.1 Am^2 [18]. Once the magnetorquer moment reaches its residual value, a magnetometer reading can be taken. The testbed has three magnetorquers arranged as an orthogonal triplet.

4.3 Thrusters

The 6× RadarSat 2 thrusters [6] were modeled as having two states, zero thrust (the thruster is off) or the nominal 1 N thrust (the thruster is on). A finite rise and fall time associated with turning the jet on or off was modelled, giving the jet a trapezoidal thrust profile as in the jet model described by [19].

5. ENVIRONMENT MODEL

5.1 Position of the Sun and the Sun Vector

The third body gravitational attraction forces from the Moon and Sun are neglected here since they are very small.

5.2 Earth's Gravitational Field

The most significant part of the perturbative force is due to the Earth's oblateness. The empirical constant used to calculate this aspect of the perturbative force is $J_2 = 1.083 \times 10^{-3}$ [20]. The J_2 perturbation is significant as it is the largest gravitational perturbation that LEO satellites experience, and its characteristic effect is responsible for the Sun-synchronicity of RADARSAT-2's orbit. This orbit provides RADARSAT-2's high power needs.

Due to its greater magnitude compared to the other harmonic terms, importance to RADARSAT-2's orbit and the simplicity with which it can be integrated into the orbital mechanics simulation, the testbed included the perturbative acceleration from Earth's oblateness and neglected other non-spherical Earth perturbations.

5.3 Earth's Atmosphere

Earth's atmosphere impacts the satellite dynamics through the aerodynamic drag generated on it. This creates a force and a torque on the satellite, and thus perturbs its orbit and attitude. Consequently, the atmosphere density local to the satellite is an important parameter. There are available models of the Earth's atmosphere. To start, the testbed used a constant value of 10^{-14} kg/m^3 for the atmosphere density from [21] based on RADARSAT-2's altitude of 798 km. This was assumed as RADARSAT-2's orbit is approximately circular ($e > 0.0006$) which is a valid approximation.

5.4 Earth's Magnetic Field

The testbed implemented a 13th order International Geomagnetic Reference Field (IGRF) model [22]. Given potential V at a position then the magnetic field, \mathbf{B} , is given by $\mathbf{B} = -\nabla V$, Eq. (4.3) describes the model implemented. Calculation of the magnetic field was in the fast dynamics loop and separately in the slower attitude estimation loop for the satellite's on-board field model. In the attitude estimation loop, calculating the magnetic field with IGRF in every cycle of the fast dynamics loop slowed the simulation. Instead, the magnetic field was calculated every 10 s. The approximate satellite position in 10 s was determined from its current position and velocity, and the magnetic field at that projected position was found. Given two positions and the magnetic field vector, a Jacobian approximated the magnetic field rate of change. Within 10 s intervals, the Jacobian interpolated the magnetic field value.

The 10 second interval significantly improved the simulation speed. A comparison of the magnetic potential from a 10 s interval interpolation against that from evaluating the power series at every time step, did not show a significant difference in the potential. The minimum spatial wavelength of the harmonic series is still large compared to the ~75 km distance the satellite travels in 10 seconds.

5.5 External Disturbance Forces and Torques

Earth Oblateness Perturbation Force

The perturbative acceleration from Earth oblateness is given in the Earth centered inertial frame [20] as in Eq. (5.1).

Gravity Gradient Torque

The gravity gradient torque is modelled in the testbed as in Eq. (5.2) [20].

Atmospheric Drag

Perturbative Force

To calculate the perturbation force due to atmospheric drag, assumptions were made: the molecules transfer all their momentum to the satellite surface (i.e., they stick to it), the speed of the air molecules is small compared to the relative speed of the satellite and the satellite's spin is negligible compared to its forward velocity [20]. Given these assumptions, the force on a flat face of the satellite is given by Eq. (5.3). Calculating this at every face, from face areas of the central bus, and summing the forces yields the perturbation force on the satellite. The areas of the solar panels were added to the +Y and -Y faces.

Perturbative Torque

To find the drag torque on the satellite, the drag force for a given face is used to calculate the drag torque from a given face using Eq. (5.4). The drag torques from each face are summed to give the total drag torque on the satellite.

Solar Radiation Pressure

Perturbative Force

Photons from the Sun strike Earth satellite surfaces, normal to the Sun, at a pressure of $p = 4.5 \times 10^{-6} \text{ N/m}^2$ [16] [20]. This imparts momentum and thus creates a force on the illuminated faces of the satellite (Eq. (5.5)). The same face areas are used as those in the drag calculations.

Perturbative Torque

The perturbative torque for each face is found using Eq. (5.4), and the torques are summed, as in the drag torque.

Magnetic Torque

The magnetic torque is proportional to the magnetic moment of the satellite, which in the testbed derives solely from the magnetorquers (whether generating a commanded moment or at their residual moment). The magnetic torque, T_M for a given magnetic moment \mathbf{M} and magnetic field \mathbf{B} is given by Eq. (5.6).

Table 2: Summary of Testbed Models

model type		reference	Eq.	model summary
sensor	gyroscope (Honeywell Miniature IMU)	[2] [12]	3.1	$\boldsymbol{\omega}_m = \boldsymbol{\omega}_{bG} + \mathbf{b}(t) + \mathbf{n}_v(t)$
	magnetometer (ZARM Technik GMA-A-75)	[2] [23]	3.2	$\mathbf{B}_m = \mathbf{B}_b + \mathbf{n}_b(t)$
	sun sensor (Adcole pyramid type)	[24]	3.3	$\begin{bmatrix} \theta \\ \varphi \end{bmatrix} = \begin{bmatrix} \text{atan}(\frac{\hat{s}_y}{\hat{s}_x}) \\ \text{atan}(\frac{\hat{s}_z}{\hat{s}_x}) \end{bmatrix} + \mathbf{n}_{ss}(t)$
	star tracker (Leonardo A-STR)	[6] [14]	3.4	$\mathbf{q}_{mST} = (\delta \mathbf{q}_{roll} \otimes (\delta \mathbf{q}_{yaw} \otimes (\delta \mathbf{q}_{pitch} \otimes \mathbf{q}_{SCIST})))$ $\mathbf{R}_{ST} = \begin{bmatrix} \sigma_{roll}^2 & 0 & 0 \\ 0 & \sigma_{pitch}^2 & 0 \\ 0 & 0 & \sigma_{yaw}^2 \end{bmatrix}$
	GPS			accuracy = ± 60 m (3σ), additive Gaussian noise with $\sigma = 20$ m
actuators	reaction wheels	[16]	4.1	$N = X_{DC} N_{em} - N_{friction}$
	magnetorquers (ZARM Technik, Sentinel-2)	[13] [2] [17]	4.2	$\mathbf{M}_c = -k_m \dot{\mathbf{B}}$ (detumbling); $\mathbf{M}_c = k_m (\mathbf{H} \times \mathbf{B})$; $\mathbf{H} = \mathbf{J} \hat{\boldsymbol{\omega}} + \mathbf{H}_w$ (momentum dumping) max moment = 150 Am^2 , linear fall time = 0.1 sec from 150 Am^2 to residual 0.1 Am^2
	jets	[6]		6×-1.0 N thrust that is on/off, finite rise and fall times
environment	Earth gravitational field			J_2 perturbation
	Earth atmosphere	[21]		fixed value, $1.17 \times 10^{-14} \text{ kg/m}^3$
	Earth magnetic field	[22]	4.3	$V(r, \theta, \varphi, t) = a \sum_{n=1}^N \sum_{m=0}^n \left(\frac{a}{r}\right)^{n+1} [g_n^m(t) \cos(m\varphi) + h_n^m(t) \sin(m\varphi)] P_n^m(\cos \theta)$
disturbance forces and torques	Earth oblateness force	[20]	5.1	$\mathbf{f}_p = \frac{3\mu J_2 R_e^2}{2r^5} [(\frac{5(\mathbf{r} \cdot \mathbf{z}_G)^2}{r^2} - 1)\mathbf{r} - 2(\mathbf{r} \cdot \mathbf{z}_G)\mathbf{z}_G]$
	gravity gradient torque	[20]	5.2	$\mathbf{T}_{gg} = \frac{3\mu}{ r ^5} \mathbf{r}_b \times \mathbf{J} \mathbf{r}_b$
	atm drag perturbing force	[20] [16]	5.3	$\mathbf{F}_{dA} = -\rho V ^2 \hat{\mathbf{V}} (\hat{\mathbf{n}} \cdot \hat{\mathbf{V}}) \mathbf{A}$
	atm drag perturbing torque	Σ 5.3	5.4	$\mathbf{T}_{dA} = \mathbf{c}_{pA} \times \mathbf{F}_{dA}$
	solar rad perturbative force	[20] [16]	5.5	$\mathbf{F}_{sA} = -(\frac{S}{I_0}) p \hat{\mathbf{S}} (\hat{\mathbf{n}} \cdot \hat{\mathbf{S}}) \mathbf{A}$
	solar rad perturbative torque	Σ 5.5		sum in the same way as in Eq. (5.4) for each face
	magnetic torque		5.6	$\mathbf{T}_M = \mathbf{M} \times \mathbf{B}$

6. STATE ESTIMATION

6.1 State Estimation using the EKF

For the spacecraft to control its position and attitude to a setpoint, it needs an estimate of its feedback position and attitude. This estimate would be derived from its sensors, accounts for sensor accuracy, integrates prior information on position and attitude, and adapts given each sensor may not return measurements at every estimation time step. For position estimation, the satellite is assumed to have only GPS. For attitude estimation, the satellite has six sensors: 1× gyroscope, 1× magnetometer, 2× Sun sensors and 2× star trackers.

For attitude determination, the star trackers are accurate, but there are conditions when they will not return a measurement. The Sun sensors and magnetometer are less prone to outages, but are less accurate, and will not return measurements under some conditions. Given this variable accuracy and availability in sensor measurements, the goal was to improve the accuracy of measurements or compensate when they are unavailable with predictions of the current attitude or position based on previous accurately measured states. A way to predict satellite states by fusing available measurements and prior states is needed for attitude and position estimation. EKF's were used for this in the testbed.

The Kalman Filter (KF) performs state estimation for a system with linear dynamics [25]. The EKF uses the same steps but for a nonlinear system and/or measurement model. Both models are linearized about the previous state vector value by taking the Jacobian, and then the EKF proceeds as described for the KF. The EKF's used for position and attitude state estimation were continuous-discrete which means the system dynamics were represented as continuous and the measurements were available at discrete times. With a discrete EKF the numerical integration of a first order differential equation is used for the prediction step, rather than a discrete transition model.

6.2 Position State Estimation

The satellite movement is represented by a state vector of its position and velocity in Earth centered inertial frame coordinates, $x = [r \ v]^T$. The process was pure Keplerian dynamics, with all other perturbation forces captured in the process noise, Q . It is straightforward to linearize the orbital equations of motion. The measurement model was also simple, given the only position sensor was the GPS, which provides position vector, r , with a known covariance.

6.3 Attitude State Estimation

The attitude state estimation EKF provides an estimate of the satellite's attitude quaternion and angular velocity vector. This can not be achieved with a standard EKF to estimate the components of the quaternion, because the quaternion's components are NOT linearly independent; the quaternion obeys a norm constraint where all its components sum in quadrature to 1. If a regular EKF was used to estimate the components, its covariance matrix would have a zero eigenvalue, and small numerical errors would cause the filter to rapidly diverge.

The solution is a "multiplicative" EKF (MEKF) [26]. The MEKF prediction step predicts the current attitude from the previous one, but the state vector being estimated contains the error quaternion representing the rotation between the predicted and the true attitude, rather than the attitude quaternion. The predicted value for this error is 0. In the update step, the measurement values are used to generate a value for this error quaternion. In a "reset" step, the updated error quaternion is multiplied by the predicted attitude to give the final attitude estimate for that time step, and the error quaternion is reset to 0. Since the attitude estimate is reset in each time step, the rotation between the predicted and true attitude is small, and the error quaternion is parameterized by a 3-vector with linearly independent components.

Another difference between the EKF used to estimate attitude and a more typical EKF is its use of gyro measurements. Rather than a dynamics model to predict the angular velocity, the MEKF implemented in the testbed uses the angular velocity vector measured by the gyroscope to propagate the kinematics. Thus, rather than being treated as a sensor, the gyroscope effectively replaces the process model. The gyroscope's drift-rate noise covariance

becomes the process (state) noise matrix Q . Since the gyroscope drifts over time, its bias vector is part of the state vector. The measured angular velocity at each time step is corrected to the true value from the estimated bias vector.

The MEKF state vector in the testbed is $x = [a \ b]^T$ where a is the small-angle three-component parameterization of the error quaternion describing the rotation from the predicted attitude to the true attitude and b is the gyroscope bias vector. At a time step, the angular velocity estimate from the previous time step is used to propagate the previous time step's estimated attitude quaternion and covariance to the current time step. The predicted current value of the state vector is $a = [0 \ 0 \ 0]^T$ (error in predicted attitude can not be predicted) and b is unchanged from the previous estimate.

In the update step, the predicted attitude quaternion is used in the measurement model to generate predicted sensor measurements. These predicted measurements are compared against the true measurements to give the innovation and the predicted covariance can be used in the standard EKF equations to give a Kalman gain. In the case of star trackers (which return an attitude quaternion) their measurement can be compared against the predicted attitude directly. Using the Kalman gain and innovation, the state vector is updated to give the 3-component parameterization a of the error quaternion and the estimate of the new gyro bias. In the reset step, the a vector is turned into a four-component error quaternion and multiplied by the predicted attitude to yield the attitude estimate for the current time step. Then the a vector component of the state vector is reset to zero. The current gyroscope measurement is corrected using the estimated bias vector to the estimated true value of the angular velocity for the current time step.

The MEKF runs at a frequency of 10 Hz. As star trackers require time to match an image to a star field, their measurements are returned with a delay taken to be 50 milliseconds in the testbed. To compensate, the MEKF is run twice in a time step; once to estimate the state at the time of the star tracker measurements with the star tracker measurements and the previous estimated state, and again to estimate the current state based on the estimate at the time of the star tracker measurement and the current values of the magnetometer and sun sensors. A more in-depth explanation of the MEKF algorithm including details of the equations is covered by Markley [10].

7. SATELLITE CONTROL

The testbed control incorporates the satellite dynamics and orbital speeds as well as the latent response of a satellite system to a set of commanded actions in an environment. The testbed satellite has reaction wheels and magnetorquers for attitude control. Reaction wheels perform planned attitude maneuvers and precision pointing whereas magnetorquers are for detumbling and momentum dumping. The control laws discussed use the attitude feedback from the state estimator. The only true state values used are the reaction wheel speeds and moments of inertia. The reaction wheel and magnetorquer control update the loop at 5 Hz – half that of the state estimator. This is like the 4 Hz for CubeSat [11], although it may be atypical for a satellite of RADARSAT-2's size.

Orbital control was achieved through on-board mission planning [27]. The relative orbital dynamics was modelled as a discrete, linear time-varying system for circular and eccentric orbits. Minimum-fuel use avoidance maneuvers are planned with linear programming. The non-linear, non-convex avoidance constraints are transformed into a time-varying sequence of linear constraints and the navigation uncertainty is applied in a worse case scenario. The mission plan is implemented by applying the satellite's thrusters.

7.1 Attitude Control

Reaction Wheels

The reaction wheel controller points the spacecraft precisely and requires a desired (setpoint) and feedback attitude from the state estimator. The orbital frame defines the desired orientation and angular velocity of the spacecraft and provides it to the control algorithm. The desired attitude is a quaternion, q_d , parameterizing a rotation from the

orbital frame to the desired orientation. If it is desired that the satellite body frame remains aligned with the orbital frame so that the SAR faces Earth and lines up along the direction of motion, then $\mathbf{q}_d = [0 \ 0 \ 0 \ 1]^T$.

Firstly, the satellite yaws to point its SAR antenna at the area of zero Doppler. To approximate this, a yaw angle was calculated for each time step to keep the SAR antenna tangent to the satellite ground track. As the satellite circles the Earth, with the Earth rotating underneath it, its ground track forms a complicated shape on the Earth's surface. At each control step, the testbed control function finds the angle between the satellite velocity component parallel to the surface of the Earth directly underneath it, and that component plus the tangential velocity of the ground underneath it (0 km/s at the Poles, $R_e \times 2\pi/day$ over the Equator). If the satellite body frame is initially aligned with the orbital frame, then this angle is the one the satellite must rotate around the orbital z-axis to have the SAR antenna (i.e. body x-axis) tangent to the ground track. This angle and axis pair are turned into a quaternion, \mathbf{q}_{turn} .

RADARSAT-2 also performs roll maneuvers of $\pm 30^\circ$ to image on either side of the ground track. These is described as a rotation of $\pm 30^\circ$ about the body x-axis and turned into a quaternion, \mathbf{q}_{slew} . RADARSAT-2 also makes yaw slews of 180° to align its thrusters for orbital adjustments, and these can be represented as a slew quaternion. These quaternions are multiplied to yield the quaternion for the rotation from the orbital to the desired frame \mathbf{q}_d (Eq. (7.1)).

$$\mathbf{q}_d = \mathbf{q}_{slew} \otimes \mathbf{q}_{turn} \quad (7.1)$$

The control law requires an error quaternion, \mathbf{q}_e , to describe the rotation from the desired to the satellite body frame. Whatever the satellite orientation, it must rotate at a rate of $2\pi/T_{orbital}$ around the orbital frame y-axis to maintain its orientation in the orbital frame. This is an angular velocity vector in the orbital frame of $[0 \ 2\pi/T_{orbital} \ 0]^T$. If the orbital to body rotation matrix is computed, this angular velocity can be transformed into the body frame and subtracted from the estimated angular velocity to yield the angular velocity error $\boldsymbol{\omega}_e$.

Reaction Wheel Control Law

There is research into attitude control techniques for spacecraft, with numerous strategies studied. More sophisticated control techniques include sliding mode control [28] [29] and model-predictive control [30]. To start, proportional-derivative (PD) and, proportional-integral-derivative (PID) control for the testbed satellite were attempted. This is not unrealistic for a RADARSAT-2 model. PID control is used in many satellites and spacecraft, from small CubeSats like ExoplanetSat [31] to larger satellites like Sentinel-2 [2] and large high-precision pointing satellites like the Hubble Space Telescope [32] [33]. RADARSAT-2 likely uses PID attitude control.

PID control proved difficult to tune, so PD control was applied, to start. PD control is also used in spacecraft attitude control [20] [11]. Eq. (7.2) is the nonlinear PD control algorithm to calculate the reaction wheel control torque.

$$\mathbf{T}_{wc} = -\mathbf{k}_p \mathbf{q}_{ev} - \mathbf{k}_d \boldsymbol{\omega}_e \quad (7.2)$$

The control torque to the reaction wheel triplet is \mathbf{T}_{wc} , with proportional gain, \mathbf{k}_p , derivative gain, \mathbf{k}_d , and \mathbf{q}_{ev} is the vector component of \mathbf{q}_e , with which $\boldsymbol{\omega}_e$ is as described. Gains \mathbf{k}_p and \mathbf{k}_d are given by Eq. (7.3) [11] [31], where ω_n is the closed-loop natural system frequency, ζ is the damping ratio and \mathbf{J} is the moment of inertia tensor.

$$\mathbf{k}_p = \omega_n^2 \mathbf{J}; \quad \mathbf{k}_d = 2\zeta \omega_n \mathbf{J} \quad (7.3)$$

The wheel control torque \mathbf{T}_{wc} is multiplied by -1 since the wheel torque has the opposite sign to the control torques.

The natural frequency and damping ratio were set largely by trial and error, although pole placement techniques [20] informed the guesses. Gain scheduling improved the performance of the reaction wheel controller [34]. When all the components of $\mathbf{q}_{ev} < 0.01$, $\omega_n = 1.1154$ rad/s and $\zeta = 1.3259$. Otherwise, $\omega_n = 0.3527$ rad/s and $\zeta = 4.1930$ – more heavily damped control. These values were obtained by first setting \mathbf{k}_p to zero and adjusting \mathbf{k}_d , until a good damping rate for a spinning satellite was achieved. Then \mathbf{k}_p was adjusted until the system maintained a single attitude.

The system was overdamped, in contrast to other spacecraft PD control systems [20]. Both natural frequencies were much less than half of the controller and estimator frequencies [11]. If the satellite’s closed-loop natural frequency is higher than the controller and estimator frequencies, it tends to oscillate at that frequency and aliasing will prevent the controller and estimator from maintaining control over the attitude and estimating the attitude correctly.

Magnetorquer Control

Detumbling is the removal of excess angular velocity so the satellite can orient itself. It is performed when the satellite first separates from its launch vehicle, or whenever the satellite has a spin rate greater than what its reaction wheels can absorb. Unlike reaction wheels, magnetorquers exert a torque on the entire satellite by torquing against the external magnetic field. B-dot [18] is a popular algorithm for detumbling (Eq. (4.2)). It is based on estimating the rate of change of the magnetic field vector from magnetometer measurements and calculating the required magnetic moment based on that rate. When the B-dot controller is running, the reaction wheels are inactive.

Reaction wheels keep the satellite pointing in the correct direction by spinning faster to absorb momentum, but they eventually saturate. To remove excess momentum and prevent the wheels from saturating, the satellite periodically ‘dumps momentum’ using the magnetorquers to impose an external torque on the satellite to counteract the effects of disturbance torques. The control law to calculate the moment for momentum dumping is Eq. (4.2).

7.2 Orbital Control

[27]’s solution for a low speed collision is briefly presented as it is the use case for the autonomy in the next section.

A challenge in satellites avoiding debris is uncertainty in the relative positioning between the two. Mueller [27] presents an on-board planning method for collision avoidance which is adopted in this testbed. Minimum fuel use avoidance maneuvers are planned with linear programming. The non-linear, non-convex avoidance constraints are transformed into a time-varying sequence of linear constraints. Consequently, the resulting maneuver can be efficiently solved, on-board the satellite, as a linear program with no integer constraints and guaranteed collision avoidance given the navigation uncertainty.

Optimal maneuver planning for collision avoidance is well studied as is the rationale for posing the optimal control problem as a linear program. The continuous time system can be discretized using a Kalman filter (Eq. (7.4)).

$$x_j = \underbrace{(A_{j-1} \dots A_1 A_0)}_{\text{state transition}} x_o + \underbrace{[A_{j-1} \dots A_1 B_0, A_{j-1} \dots A_2 B_1, \dots, A_{j-1} B_{j-2}, 0]}_{\text{input matrix}} \begin{bmatrix} u_o \\ u_1 \\ \vdots \\ u_{j-2} \\ u_{j-1} \\ \vdots \\ u_{N-1} \end{bmatrix} \quad (7.4)$$

$$x_j = H_j x_o + G_j \bar{u}$$

The accelerations, \bar{u} , are the decision variables in the optimal control problem. They are constrained to lie in the non-negative quadrant.... by partitioning the control into a positive and negative component as follows:

$$\bar{u} = \begin{bmatrix} \bar{u}^- \\ \bar{u}^+ \end{bmatrix}. \quad (7.5)$$

Defining $\bar{G}_j = [-G_j, G_j]$, the relationship between the j^{th} state and the control vector becomes:

$$x_j = H_j x_o - G_j \bar{u}^- + G_j \bar{u}^+ = H_j x_o + \bar{G}_j \bar{u}. \quad (7.6)$$

This doubles the dimension of the control vector but allows it to be expressed as a linear program. Then, the optimization problem is stated as follows: given an initial relative object state, determine a control history that minimizes the required fuel subject to a) maintain a minimum stand-off distance, d , from the object and b) meet the prescribed station-keeping constraints. Generally, the compact formulation is:

$$\begin{aligned} \text{minimize:} & \quad \|\bar{u}\|_1 \\ \text{subject to:} & \quad a_i^T \bar{u} - b_i \leq 0, i = 1, \dots, M; \quad \bar{u} \geq 0 \end{aligned}$$

such that a_i, b are the linear data for the i^{th} constraint. Defining a 1-norm for the cost applies an equal penalty to every control at every time step yields Eq. (7.7).

$$\|\bar{u}\|_1 = \sum_{i=1}^{6N} \bar{u}_i \quad (7.7)$$

In low speed collisions the satellite and debris are in similar orbits. [27] stipulates the satellite maintain a minimum stand-off distance from the debris. This is realized by enforcing the constraint (Eq. (7.8)):

$$ax^2 + by^2 + cs^2 \geq d^2 \quad (7.8)$$

which defines an exclusion ellipsoidal zone around the debris to avoid. Given this exclusion zone, the collision avoidance strategy is as follows:

1. separation guidance: exit the avoidance region and
2. nominal guidance: stay out of the avoidance region.

The semi-major axis, d , of the ellipsoidal volume can be adjusted during the mission. Mueller assumes $d = 60$ meters. A buffer of $m = 30$ meters beyond the avoidance region defines the nominal boundary. Nominal guidance keeps the satellite outside of the nominal boundary so small errors do not create unwanted re-entry of the avoidance region.

7.2.1 Separation Guidance

The linear constraints of state vector, x_n , that capture the separation guidance strategy objectives are as follows:

1. exit the avoidance region with a specified time, T_{exit}
2. do not get any closer than the initial position and
3. do not re-enter the region.

The resulting compact formulation of the linear program for the separation guidance problem is as follows:

$$\begin{aligned} \text{minimize:} & \quad \|\bar{u}\|_1 \\ \text{subject to:} & \quad a_i^T \bar{u} - b_i + s_i = 0 \quad i = 1, \dots, M; \quad \bar{u} \geq 0; s \geq 0 \end{aligned}$$

7.2.2 Nominal Guidance

If the satellite is outside of the avoidance region then the objective is to maintain a relative trajectory that does not re-enter the region. A “safe ellipse” is defined which is a passive relative trajectory that remains outside of the avoidance region even in the presence of along-track drift. The safe ellipse trajectory surrounds the circular projection of the avoidance region in the cross-track / radial plane. This is governed by the following constraint:

$$y^2 + z^2 \geq (d + m)^2 \quad (7.9)$$

As this is non-linear and non-convex it must be re-posed so it is within the context of a linear program. This is achieved by approximating the region as a time-varying sequence of linear constraints. A non-convex region can be approximated by a convex half-space tangent to the region whose orientation changes with time [27]. This format creates a convex feasible space for the problem, at each time step, and facilitates additive linearized station-keeping constraints. In this way, the satellite is driven to a safe relative trajectory with only linear constraints and thus the problem is posed as a pure linear program that is tractable and quickly solvable.

The nominal guidance problem is thus:

$$\begin{aligned} &\text{minimize:} && \|\bar{u}\|_1 \\ &\text{subject to:} && \mathbf{q}_3^T \bar{G}_N \bar{u} + \mathbf{q}_3^T Hx_0 - d - \epsilon_D \leq 0 \\ & && -\mathbf{q}_3^T \bar{G}_N \bar{u} + \mathbf{q}_3^T Hx_0 - d - \epsilon_D \leq 0 \\ & && \mathbf{q}_6^T \bar{G}_j \bar{u} + \mathbf{q}_6^T Hx_0 - (d + m) \leq 0, \quad j = K, \dots, N \end{aligned}$$

8. TESTBED VALIDATION

As mentioned earlier, every satellite possesses some level of autonomy to respond to situations when it is not in contact with its GCS. For the testbed satellite, three simplified modes were defined: mode 1 is detumbling, mode 2 is momentum dumping and mode 3 is nominal operations. The satellite is in mode 1 if it senses any component of the total angular momentum is above 18 Nms (max reaction wheel momentum storage). In this mode it shuts down the reaction wheel controller and runs the B-dot algorithm. The satellite is in mode 2 if the total angular momentum components are less than 18 Nms but any of them are above 9 Nms. In this mode the reaction wheel and momentum dumping controller engages. Otherwise the satellite is in mode 3, where the reaction wheel controller is active and the magnetorquers are not used. The satellite should maintain its desired attitude and perform any required slews if it is in mode 2 or 3. Modes 3 and 1 are demonstrated.

8.1 Attitude Maneuvers (Small Disturbance Case)

The predicted results from the testbed were compared against RADARSAT-2 responses for a given mission (Table 3). The satellite starts with its body frame aligned with the orbit frame. Throughout the orbit it was commanded to slowly rotate about the orbital frame z-axis to maintain its SAR alignment with its ground track. Initially, there were no slew commands (other than keep the SAR aligned). The simulation was run for 6050 seconds (~ 1 orbit) with a time step of 0.005 seconds. To test the attitude control, the satellite was commanded to perform a series of attitude maneuvers. Slew maneuvers and disturbances were superimposed on this.

Table 3: Satellite mission for testbed simulation

mission time (seconds)	satellite commands	reason
1500	adjust attitude to 29.8 ° roll angle	SAR images one side of the ground track
2500	apply torque for 0.005 seconds: [1800 Nm 1800 Nm 1800 Nm] ^T	small disturbance of 9 Nms angular momentum applied to each satellite axis
3000	adjust attitude to -29.8 ° roll angle	SAR images other side of the ground track
4500	return to 0° roll	slew maneuver in preparation for an orbital maneuver
	rotate 180° about yaw axis	

Fig. 3 shows the 3 components of the vector part of the attitude estimate error quaternion and Fig. 4 shows the same for the control error quaternions. RADARSAT-2's 3σ limits are marked on the plots as a reference. The attitude estimate seems to accurately match RADARSAT-2's attitude determination accuracy. The control accuracy is somewhat close to RADARSAT-2's control accuracy. In the full-sized control error quaternion plots, the effect of the disturbance torque on the satellite attitude is visible as a spike at 2500 seconds, but the satellite quickly steers back to the correct attitude given it is a small disturbance to start with.

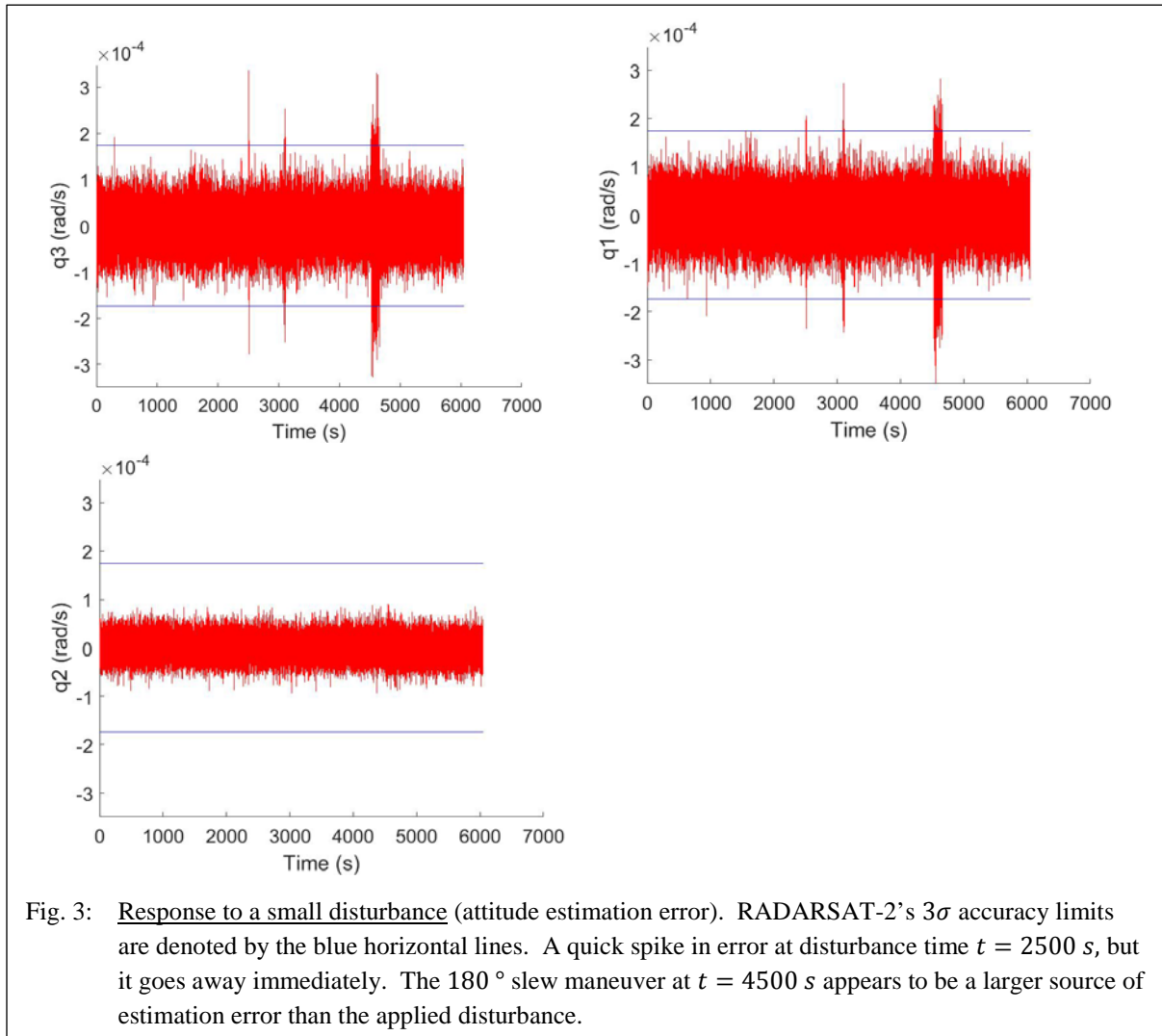
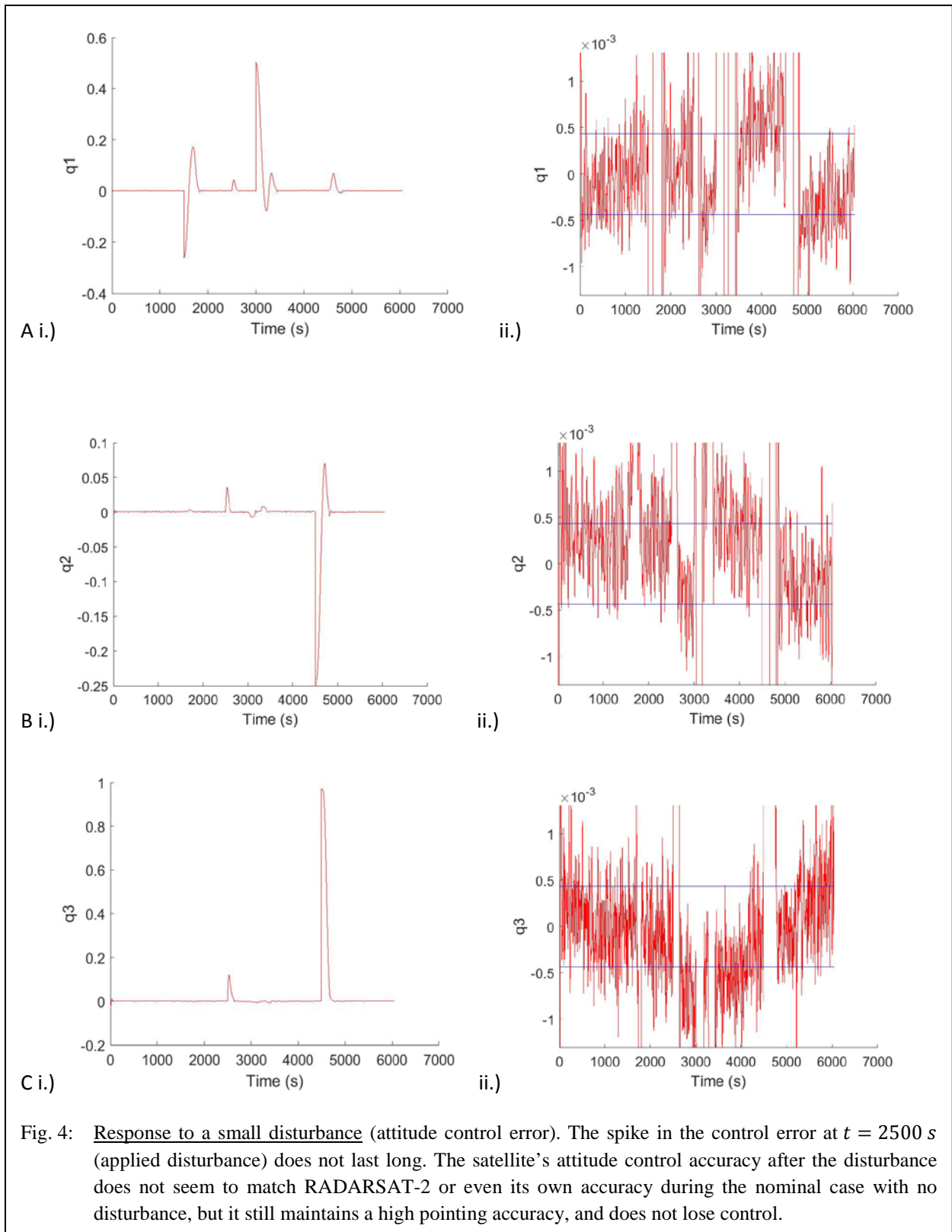


Fig. 3: Response to a small disturbance (attitude estimation error). RADARSAT-2's 3σ accuracy limits are denoted by the blue horizontal lines. A quick spike in error at disturbance time $t = 2500$ s, but it goes away immediately. The 180° slew maneuver at $t = 4500$ s appears to be a larger source of estimation error than the applied disturbance.

8.2 Attitude Maneuvers (Large Disturbance Case)

Again, the predicted results from the testbed were compared against RADARSAT-2 responses for a given mission. The mission plan was the same as that in Table 3 with the exception that at $t = 2500$ s a large impulsive torque, $[5400 \text{ Nm } 5400 \text{ Nm } 5400 \text{ Nm}]^T$, was applied to the satellite to add 27 Nms of angular momentum to each satellite axis for 0.005 seconds. This objective was to assess the satellite's detumbling performance. This large disturbance case ran for 54,450 seconds or ~ 9 orbits. Fig. 5 shows the satellite angular velocity. At the instance of the disturbance, the satellite immediately experiences an impulse in its angular velocity. It starts tumbling around one axis, but then initiates detumbling mode and over the course of the time span detumbles itself, to the point that at the end of the interval it has recovered and is at its nominal angular velocity.



The response of the model to a small and large disturbance, superimposed on a nominal imaging mission (commanded attitude and slew changes), appear to be within the expectations of a RADARSAT-2 like satellite.

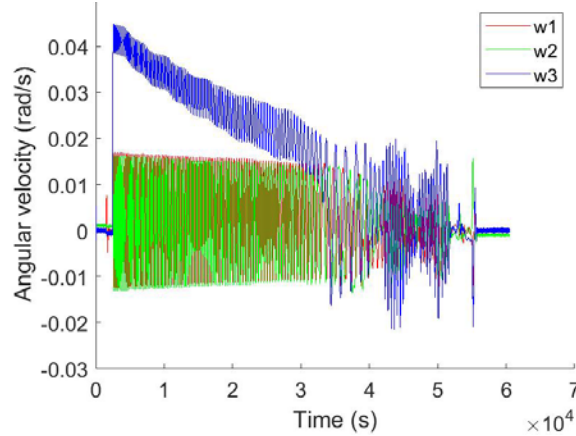


Fig. 5: Response to a large disturbance. The three components of the satellite's angular velocity, W_1 , W_2 and W_3 , over 9 orbits. The disturbance causes a massive impulse in the satellite's angular momentum and it begins to tumble around its most stable axis at a high rate. Detumbling mode is initiated and the magnetorquers act to counteract the motion and detumble the satellite. At the far-right of the plot, after about 9 orbits, the satellite is mostly back in its nominal regime.

8.3 Orbital Maneuvers

Fig. 6 shows the response of the satellite to orbital adjustments from the planner to avoid collision with debris. For the case where the debris is 80 m from the satellite (Fig. 6a), the orbital adjustment went directly to a nominal maneuver as no additional separation was needed. Note the nominal maneuver drifts away from the debris.

For the case where the satellite is inside the exclusion zone (10 m offset from debris, Fig. 6b), note the satellite correctly first performs the separation maneuver to increase the satellite-debris stand-off to 60 m along-track and then performs a nominal maneuver which drifts away from the debris.

The actuation of the orbital adjustments differs from Mueller's [27]. As in RADARSAT-2, the testbed uses impulsive thrusters whereas Mueller used continuous thrust. Mueller's satellite can thrust in all 3 translational degrees-of-freedom. RADARSAT-2's jets only thrust in the satellite centered inertial +x and +y directions. The assumption is that the planned orbital maneuver is available immediately and that it takes 600 seconds to complete an attitude adjustment. Then, 2 minutes is needed to achieve the final applied impulse. Therefore, 12 minutes total is needed to realize a thruster impulse in response to a commanded maneuver. Thrusters are applied every 10 minutes as needed. When there is a separation and nominal maneuver, the position after the separation is used to plan the nominal maneuver. It is assumed the satellite knows its position well (i.e. no uncertainty). Given adjustments made to capture

RADARSAT-2, the results generally agree with Mueller's. This is the best that can be done to verify that the orbital planner is meeting its objectives. The application of this testbed as a tool to assess autonomy is discussed next.

9. AUTONOMY

As mentioned earlier, the testbed can evaluate situations that are less straightforward through existing tools [7] [8]. These situations range from satellite responses to late collision warnings, collision avoidance with objects that are too small to track with ground radar, varying communications failure between the satellite and GCS, and failed actuators. This section will introduce the work underway towards late collision warnings and autonomous responses to collision avoidance with small debris.

9.1 Late Collision Warnings

For late collision warnings, the testbed varied debris detection times from early to late, relative to an orbit, and observed the response to commanded satellite avoidance maneuvers. The satellite fuel consumption versus the warning time was modelled for incoming along-track, cross-track and radial debris relative collision speeds. Incoming debris was oriented so that RADARSAT-2 had to make attitude changes to fully push the testbed. The warning time was studied at time increments of 10, 15, 25, 50, 75 and 100% of a 6000 second LEO orbit. Not unexpectedly, if the orbital adjustment was realized with ample warning time, the Δv burn to avoid a collision, in terms of fuel consumed is less (Fig. 7). Without exception, it was not possible to avoid a collision given 15 minutes of warning. Beyond a certain point in the warning time, the fuel consumed will not change appreciably. There is a trade-off as a collision avoidance maneuver far advanced in time adds to the satellite position uncertainty at the projected collision time.

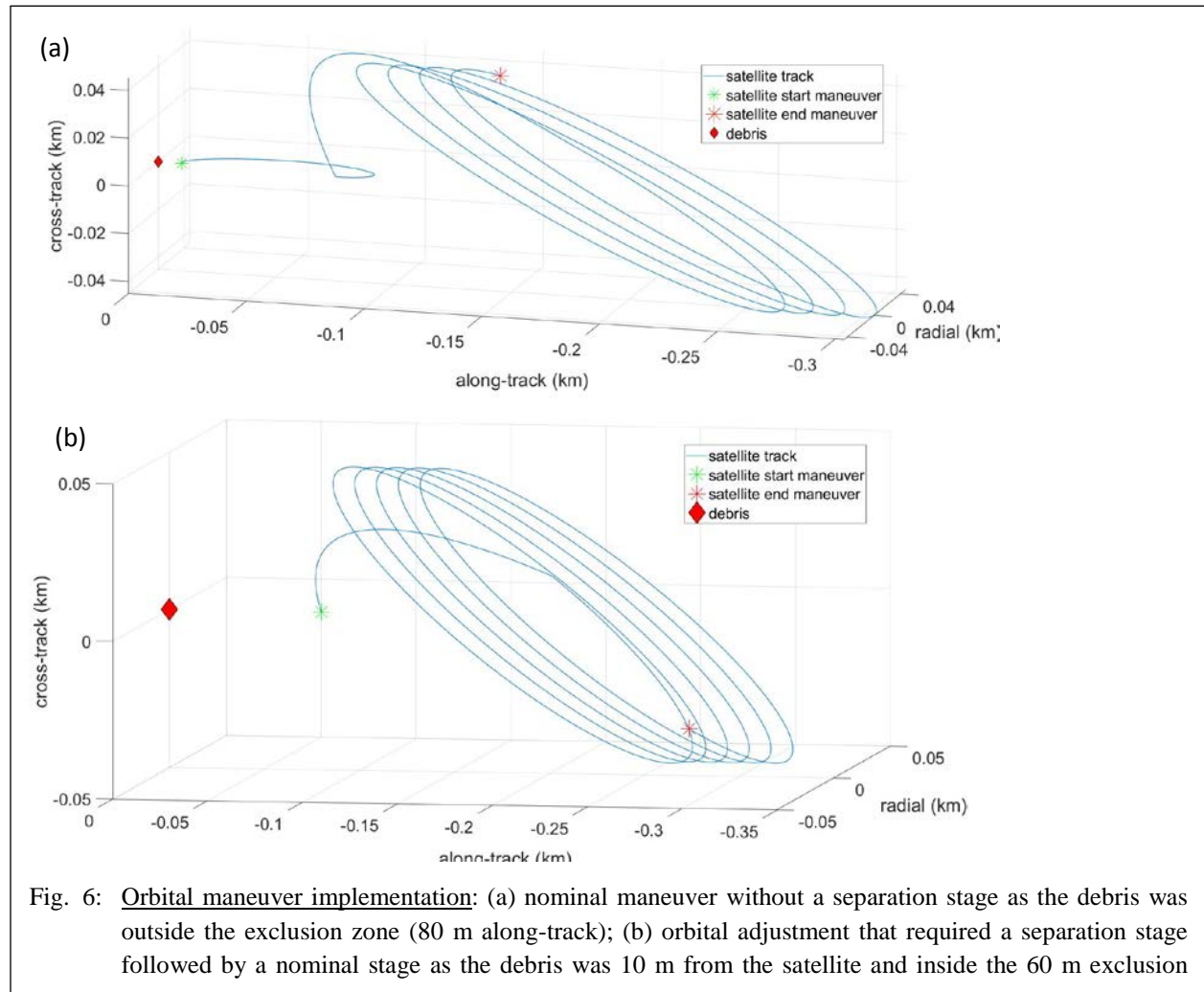


Fig. 6: Orbital maneuver implementation: (a) nominal maneuver without a separation stage as the debris was outside the exclusion zone (80 m along-track); (b) orbital adjustment that required a separation stage followed by a nominal stage as the debris was 10 m from the satellite and inside the 60 m exclusion

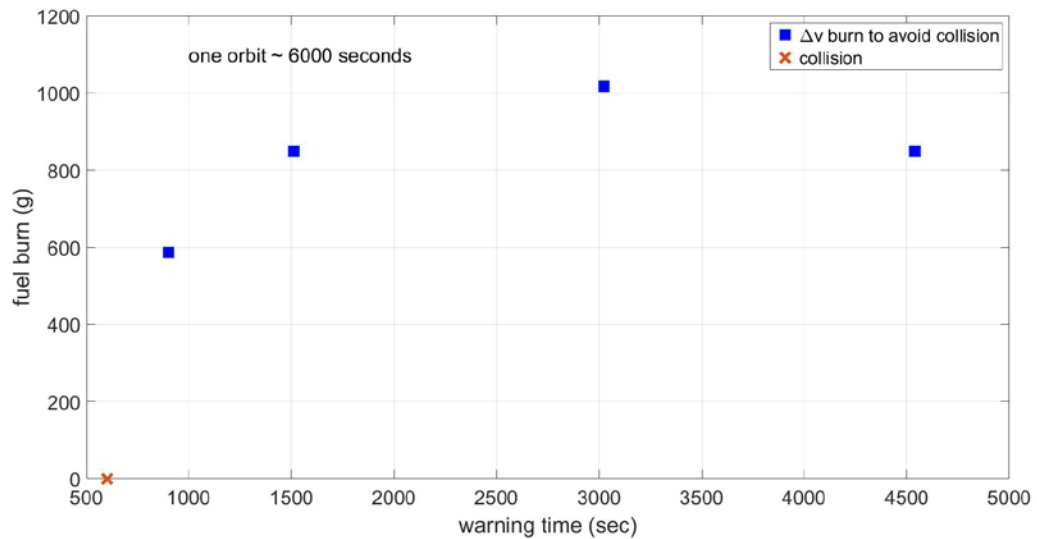


Fig. 7: Fuel burn to avoid incoming cross-track collisions at relative speeds of 50 m/s. At $t = 900$ seconds, the satellite collided with the debris.

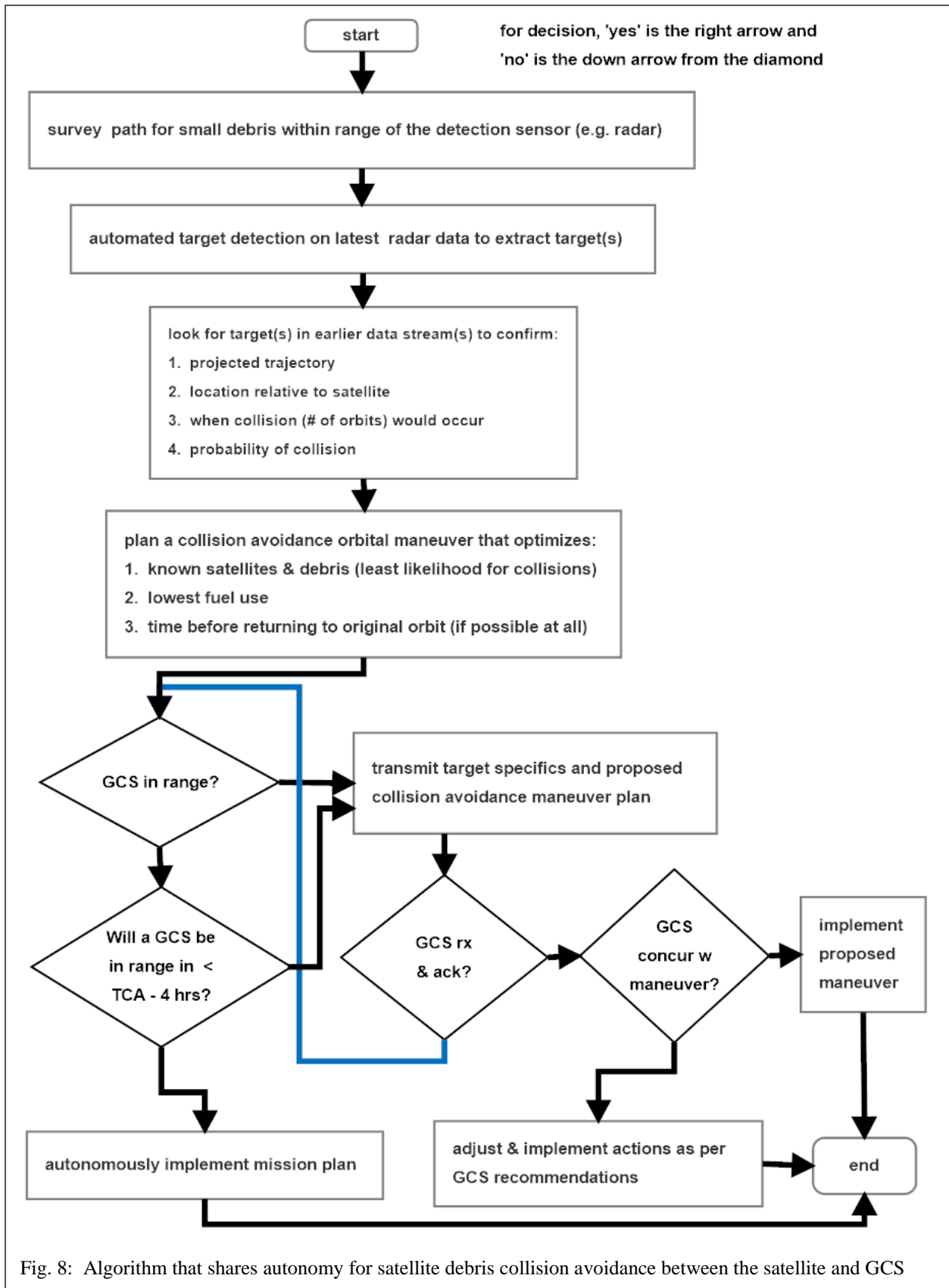
9.2 Architecture for Autonomous Satellite Debris Avoidance

Fig. 8 shows a distributed autonomy algorithm for satellite debris avoidance. In the first step the on-board radar sensor surveys the satellite path. Then, automated target detection is applied to the survey data stream to detect small ($< 5\text{-}10$ cm) targets. If candidate target(s) are found, previous sensor data streams, for the same part of the orbit, are re-analyzed to see if the targets were visible then. If not, the radar is re-aimed to focus on the potential target(s) locations for the next survey data collection in that part of the orbit. The intent is to confirm the target(s) existence, determine their location relative to the satellite, project their trajectory, calculate a likelihood of collision and when the collision (in number of orbits) might occur. Then, an orbital maneuver is planned to avoid the collision. The results of the in-situ detection, analysis, and planned orbital adjustment is formed into a message to transmit to the GCS.

Then, the algorithm determines when the next GCS is in range. It compares that to the time $TCA - 4$ hours (for instance), the latest that the orbital maneuver should be implemented. If that time is greater than $TCA - 4$ hours, then the satellite will transmit it when the GCS is in range. After the satellite transmits the message it waits for an acknowledgement from the GCS and whether the GCS concurs with the proposed avoidance maneuver and timing. If GCS does, the satellite will implement the maneuver. If GCS does not concur with the proposed maneuver, then it makes a recommendation and transmits it to the satellite. The GCS autonomy end will look at the detected target information and may decide on a different avoidance maneuver. The satellite implements what the GCS sends back.

If the satellite does not get a 'message receive' acknowledgement from the GCS, it continues to transmit at every opportunity. When the time is at $TCA - 4$ hours and still no reply, the satellite autonomously performs the maneuver.

There is value to the proposed algorithm, however, this is not clearly quantified yet and is the topic of future work.



CONCLUDING REMARKS

A flexible testbed for assessing satellite control (all levels of autonomy) was developed and tested against RADARSAT-2 known responses. The testbed captures the dynamics of the satellite and can model its sensors, actuators, environment, position estimation and control. The testbed is more flexible and adaptable than existing distributed testbeds. This flexibility and fidelity is required for assessing autonomy where the physical satellite form and dynamics, sensors, actuators, mission-planner, positioning, control and environment can interact very closely with the autonomy. The validation for attitude control under small and large disturbances for nominal and detumbling operations were encouraging. The planner for orbital maneuvers also appears to work as desired. Then, the testbed was applied to the problem of determining how far in advance an avoidance maneuver should be realized and the consequent impact on fuel consumption. Future work will have the testbed address autonomous avoidance maneuvers given that most of the algorithmic components are developed.

The testbed can be used to assess a variety of satellite autonomy algorithms, in addition to autonomous satellite avoidance, with the intent to assess the value of autonomy that is distributed between the satellite and the ground control station.

REFERENCES

- [1] Z. Ali, G. Kroupnik, G. Matharu, J. Graham, I. Barnard, P. Fox and G. Raimondo, "RADARSAT-2 space segment design and its enhanced capabilities with respect to RADARSAT-1," *Canadian Journal of Remote Sensing*, 2004.
- [2] G. Wiedermann, S. Winkler, G. Wiedermann, W. Gockel, S. Winkler, J. M. Rieber, B. Kraft and D. Reggio, "The Sentinel-2 satellite attitude control system - challenges and solutions," in *GNC 2014: 9th International Conference on Guidance, Navigation and Control Systems*, Porto, Portugal, 2014.
- [3] T. Yairi, Y. Kawahara, R. Fujimaki, Y. Sato and K. Machida, "Telemetry-mining: a machine learning approach to anomaly detection and fault diagnosis for space systems," in *2nd IEEE Int. Conf. Space Mission Challenges for Information Technology*, 2006.
- [4] M. J. Berkowitz, A. A. Kelsey and G. Swietek, "Space mission resilience," in *AIAA SPACE 2013 Conference and Exposition*, 2013.
- [5] A. Houpert, "A Space Based Radar on a Micro-Satellite for In-Situ Detection of Small Orbital Debris," *Acta Astronautica*, vol. 44, no. 7-12, pp. 313-321, 1999.
- [6] H. J. Kramer, "eoPortal: RADARSAT-2," ESA, [Online]. Available: <https://directory.eoportal.org/web/eoportal/satellite-missions/r/radarsat-2>. [Accessed 20 May 2018].
- [7] *STK SOLIS*.
- [8] *42: A Comprehensive General-Purpose Simulation of Attitude and Trajectory Dynamics and Control of Multiple Spacecraft Composed of Multiple Rigid or Flexible Bodies*.
- [9] C. Livingstone, I. Sikaneta, C. Gierull, S. Chiu and P. Beaulne, "RADARSAT-2 system and mode description," DRDC, 2005.
- [10] F. L. Markley, "Attitude Error Representations for Kalman Filtering," *Journal of Guidance, Control, and Dynamics*, 2003.
- [11] E. Wise and D. Miller, "Design, analysis and testing of a precision guidance, navigation and control system for a dual-spinning CubeSat," MIT, Cambridge, 2013.
- [12] Honeywell International, "MIMU: Miniature inertial measurement unit," Honeywell International, 2003.
- [13] ZARM Technik AG, "ZARM Technik Attitude Control System," ZARM Technik AG, [Online]. Available: <https://www.zarm-technik.de/products/>. [Accessed 27 May 2018].
- [14] F. Boldrini, "Leonardo Star Trackers -Flight Experiences and Introduction of SPACESTAR Product

- on GEO Platforms," in *11th ESA Workshop on Avionics, Data Control and Software Systems*, 2017.
- [15] Leonardo Airborne and Space Systems, "A-STR and AA-STR Autonomous Star Trackers," Leonardo, 2016. [Online]. Available: <http://www.leonardocompany.com/en/-/aastr>. [Accessed 3 May 2018].
- [16] J. Wertz, Ed., *Spacecraft Attitude Determination and Control*, Springer, 1978.
- [17] NewSpace Systems, "Magnetorquer Rod," 2018. [Online]. Available: http://www.newspacesystems.com/wp-content/uploads/2018/02/NewSpace-Magnetorquer-Rod_6a-1.pdf. [Accessed 13 May 2018].
- [18] D. Guerrant, "Design and analysis of fully magnetic control for picosatellite stabilization," California Polytechnic State University, San Luis Obispo, CA, 2005.
- [19] Computer Sciences Corporation, *Spacecraft Attitude Determination and Control*, J. R. Wertz, Ed., Dordrecht: D. Reidel Publishing Company, 1978.
- [20] A. H. De Ruiter, C. J. Damaren and J. R. Forbes, *Spacecraft Dynamics and Control: An Introduction*, Chichester: John Wiley & Sons, Ltd., 2013.
- [21] K. S. Champion, A. E. Cole and A. J. Kantor, "Chapter 14: Standard and Reference Atmospheres," in *Handbook of Geophysics and the Space Environment*, A. S. Jursa, Ed., United States Air Force, 1985.
- [22] I. D. V-Mod, "International Geomagnetic Reference Field," NOAA, 22 December 2014. [Online]. Available: <https://www.ngdc.noaa.gov/IAGA/vmod/igrf.html>. [Accessed 26 May 2018].
- [23] O. J. Woodman, *An introduction to inertial navigation*, Cambridge University, 2007.
- [24] Adcole Corporation, "Coarse Sun Sensor Pyramid".
- [25] M. S. Grewal and A. P. Andrews, *Kalman Filtering: Theory and Practice Using MATLAB*, 3 ed., Wiley-IEEE Press, 2008.
- [26] E. Lefferts, F. Markely and M. Shuster, "Kalman filtering for spacecraft attitude estimation," *Journal of Guidance, Control and Dynamics*, vol. 5, no. 5, 1982.
- [27] J. B. Mueller, "Onboard Planning of Collision Avoidance Maneuvers Using Robust Optimization," in *AIAA Unmanned...Unlimited Conference*, Seattle, WA, 2009.
- [28] H. Bang, C.-K. Ha and J. Hyoun Kim, "Flexible spacecraft attitude maneuver by application of sliding mode control," *Acta Astronautica*, 2005.
- [29] C. Pukdeboon and A. S. Zinober, "Control Lyapunov function optimal sliding mode controllers for attitude tracking of spacecraft," *Journal of the Franklin Institute*, 2012.
- [30] Ø. Hegrenæs, J. T. Gravdahl and P. Tøndel, "Spacecraft attitude control using explicit model predictive control," *Automatica*, 2005.
- [31] C. M. Pong and D. W. Miller, "High-Precision Pointing and Attitude Estimation and Control Algorithms for Hardware-Constrained Spacecraft," 2014.
- [32] W. G. Frazier and D. A. Lawrence, "Controller redesign for the Hubble Space Telescope," NASA, 1993.
- [33] S. Hur-Diaz, J. Wirzburger and D. Smith, "Three axis control of the Hubble Space Telescope using two reaction wheels and magnetic torquer bars for science observations," in *Advances in the Astronautical Sciences*, 2008.
- [34] B. Streetman, "Attitude Tracking Control Simulating the Hubble Space Telescope," 2003.
- [35] P. McMahan and R. Laven, "Results from ten years of reaction/momentum wheel life testing," in *11th European Space Mechanisms and Tribology Symposium*, 2005.
- [36] E. Thebault, "International Geomagnetic Reference Field: the 12th generation," *Earth, Planets and Space*, vol. 67, 2015.

- [37] D. E. Winch, D. J. Ivers, J. P. Turner and R. Stening, "Geomagnetism and Schmidt quasi-normalization," *Geophysical Journal International*, 2005.
- [38] J. M. Piccone, A. E. Hedin, D. P. Drob and A. C. Aikin, "NRLMSISE-00 empirical model of the atmosphere: Statistical comparisons and scientific issues," *Geophysical Research: Space Physics*, 2002.

NOMENCLATURE

(vectors / matrices are bolded)

Eq.	symbol	definition
3.1	ω_m	measured body frame angular velocity rel to inertial frame (expressed in body frame)
	$\mathbf{n}_v(\mathbf{t})$	drift rate noise, $\mathbf{n}_v(\mathbf{t}) \sim N(\mathbf{0}_{3 \times 1}, \sigma_y^2 \mathbf{I}_{3 \times 3})$
	$\mathbf{b}(\mathbf{t})$	gyroscope drift-rate bias vector, $\dot{\mathbf{b}} = \mathbf{n}_u(\mathbf{t})$
	$\mathbf{n}_u(\mathbf{t})$	$\mathbf{n}_u(\mathbf{t}) \sim N(\mathbf{0}_{3 \times 1}, \sigma_u^2 \mathbf{I}_{3 \times 3})$
3.2	\mathbf{B}_m	measured magnetic field
	\mathbf{B}_b	true magnetic field in the body frame
	$\mathbf{n}_b(\mathbf{t})$	$\mathbf{n}_b(\mathbf{t}) \sim N(\mathbf{0}_{3 \times 1}, \sigma_b^2 \mathbf{I}_{3 \times 3})$
3.3	A	area of flat face on satellite
	θ	Sun right ascension angle (sensor frame)
	ϕ	Sun declination angle (sensor frame)
	S	magnitude of sun vector
	$\tilde{\mathbf{S}}$	transformed sun unit vector
	I_o	solar irradiance at 1 AU
	$\mathbf{n}_{ss}(\mathbf{t})$	accuracy of the Sun sensor, $\mathbf{n}_{ss}(\mathbf{t}) = \sim N(\mathbf{0}_{2 \times 1}, \sigma_{ss}^2 \mathbf{I}_{2 \times 2}), \sigma_{ss} = \pm 2^\circ\text{C}$
3.4	\mathbf{q}_{mST}	measured star tracker quaternion
	$\delta \mathbf{q}_{dof}$	Euler angle errors: $\theta_{roll} \sim N(0, \sigma_{roll}), \phi_{pitch} \sim N(0, \sigma_{pitch}), \psi_{yaw} \sim N(0, \sigma_{yaw})$ converted to $\delta \mathbf{q}_{dof}$
	\mathbf{q}_{st}	star tracker quaternion
	\mathbf{q}_{SCIST}	true quaternion for rotation from SCI to star tracker frame, $\mathbf{q}_{SCIST} = \mathbf{q}_{ST} \otimes \mathbf{q}$
4.1	N	net torque
	X_{DC}	duty cycle of pulses applied to reaction wheel (-1, 1)
	N_{em}	applied electromotive for duty cycle unity, $N_{em} = 2N_o \alpha r (a^2 + r^2)^{-1}$
	N_o	maximum magnitude of N_{em} ; $N_o = 0.3 \text{ Nm}$ (RADARSAT-1 [35])
	r	$r = 1 - s/s_{max}$ for $X_{DC} > 0$ $r = 1 + s/s_{max}$ for $X_{DC} < 0$
	s	reaction wheel speed; $s_{max} = 4000 \text{ rpm}$; (MOOG Bradford W18 for Sentinel-1 [2])
	s_{max}	the maximum wheel speed;
	α	value of s when $N_{em} = N_o$; occurs at $s = s_{max}/2$ [16]

Eq.	symbol	definition
	N_c	Coulomb friction coeff; $N_c = 7.06 \times 10^{-4} Nm \times 10$ ([16] based on wheel with 1/10 th torque)
	f	viscous friction coeff; $f = 1.21 \times 110^{-6} Nm/rpm \times 10$ ([16] based on wheel with 1/10 th torque)
	$N_{friction}$	$N_{friction} = N_c sign(s) + fs$
	J_w	moment of inertial; $J_w = 0.0430 kg m^2$ (MOOG Bradford W18 for Sentinel-1 [2])
4.2	\mathbf{M}_c	calculated magnetic moment to request from the magnetorquer
	$\dot{\mathbf{B}}$	rate of change of the magnetic field vector estimated from the current and previous measurements
	\mathbf{H}	total angular momentum vector of the satellite and reaction wheels
	k_m	control gain, $k_m = 3 \times 10^9$ (detumbling); $k_m = 1.5 \times 10^6$ (momentum dumping)
	H_w	reaction wheel angular momentum
4.3	V	Earth's magnetic potential at a given position
	(r, θ, φ)	spherical coordinate system that rotates with the Earth
	θ	geocentric co-latitude
	r	distance from the centre of the Earth
	φ	east longitude
	a	Earth reference radius = 6371.2 km
	g_n^m, h_n^m	empirically derived coefficients in units of nanoTesela [36]
	P_n^m	Schmidt quasi-normalized associated Legendre function of degree n and order m [37] [37]
	N	order of series approximation, coefficient available up to 13
5.1	z_G	unit vector of Earth Centered inertial frame z-axis
	R_e	radius of Earth
	J_2	1.083×10^{-3}
5.2	\mathbf{r}_b	satellite position vector in body coordinates
5.3	ρ	density of air
	\mathbf{V}	satellite velocity
	$\hat{\mathbf{V}}$	unit velocity
	$\hat{\mathbf{n}}$	unit vector normal to flat face of the satellite
	A	area of one flat face of the satellite
5.4	\mathbf{c}_{PA}	vector points from satellite centre of mass to centre of rectangular face, A
3.3	p	$4.5 \times 10^{-6} N/m^2$